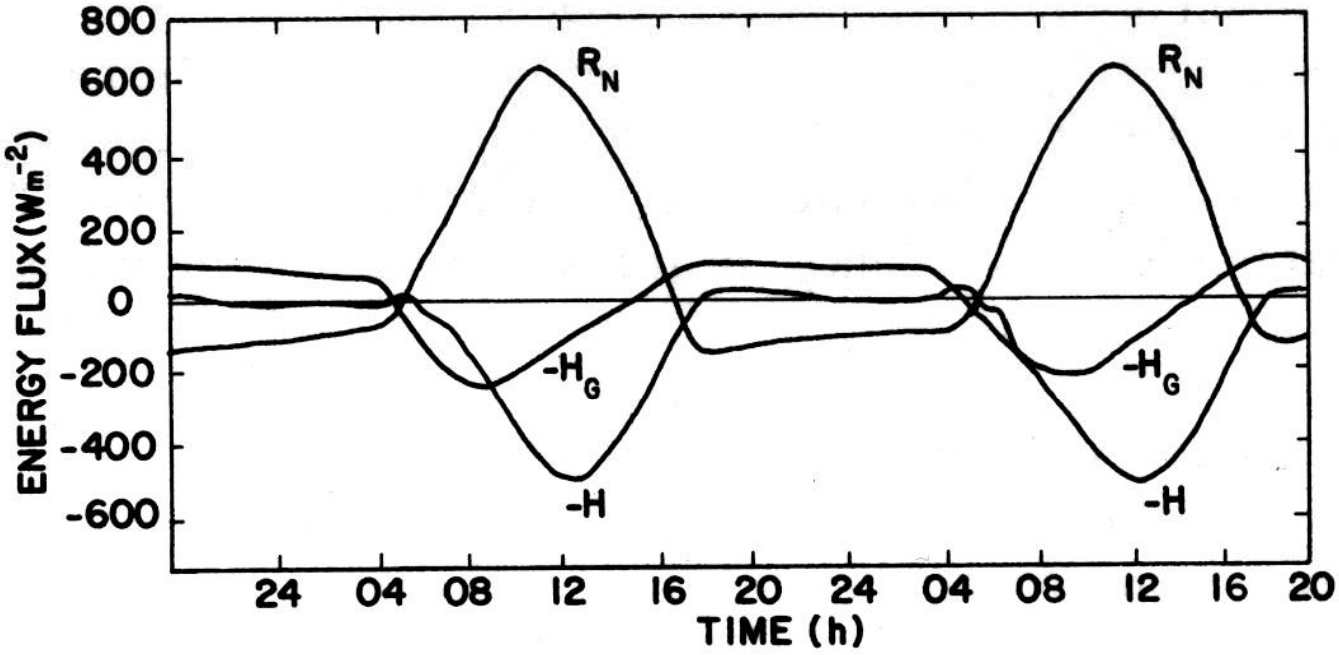

Figure 2.3 Observed diurnal energy budget over a dry lake bed at El Mirage, California, on June 10–11, 1950. [After Vehrencamp (1953).]

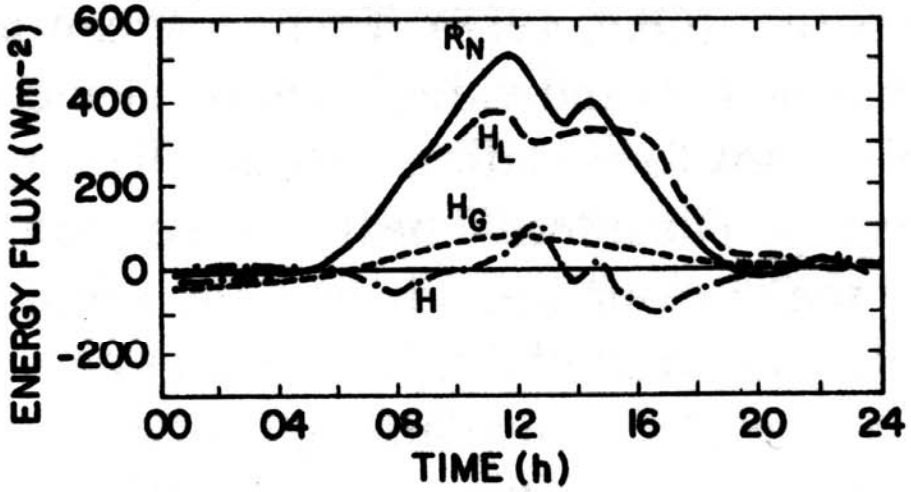

Figure 2.4 Observed diurnal energy budget of a barley field at Rothamsted, England, on July 23, 1963. [From Oke (1987); after Long *et al.* (1964).]

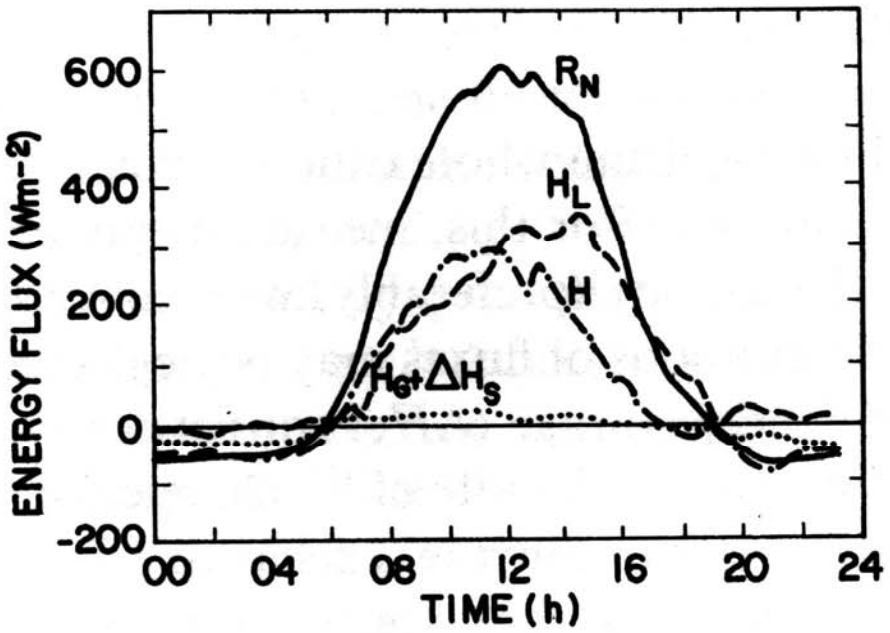

Figure 2.5 Observed energy budget of a Douglas fir canopy at Haney, British Columbia, on July 23, 1970. [From Oke (1987); after McNaughton and Black (1973).]

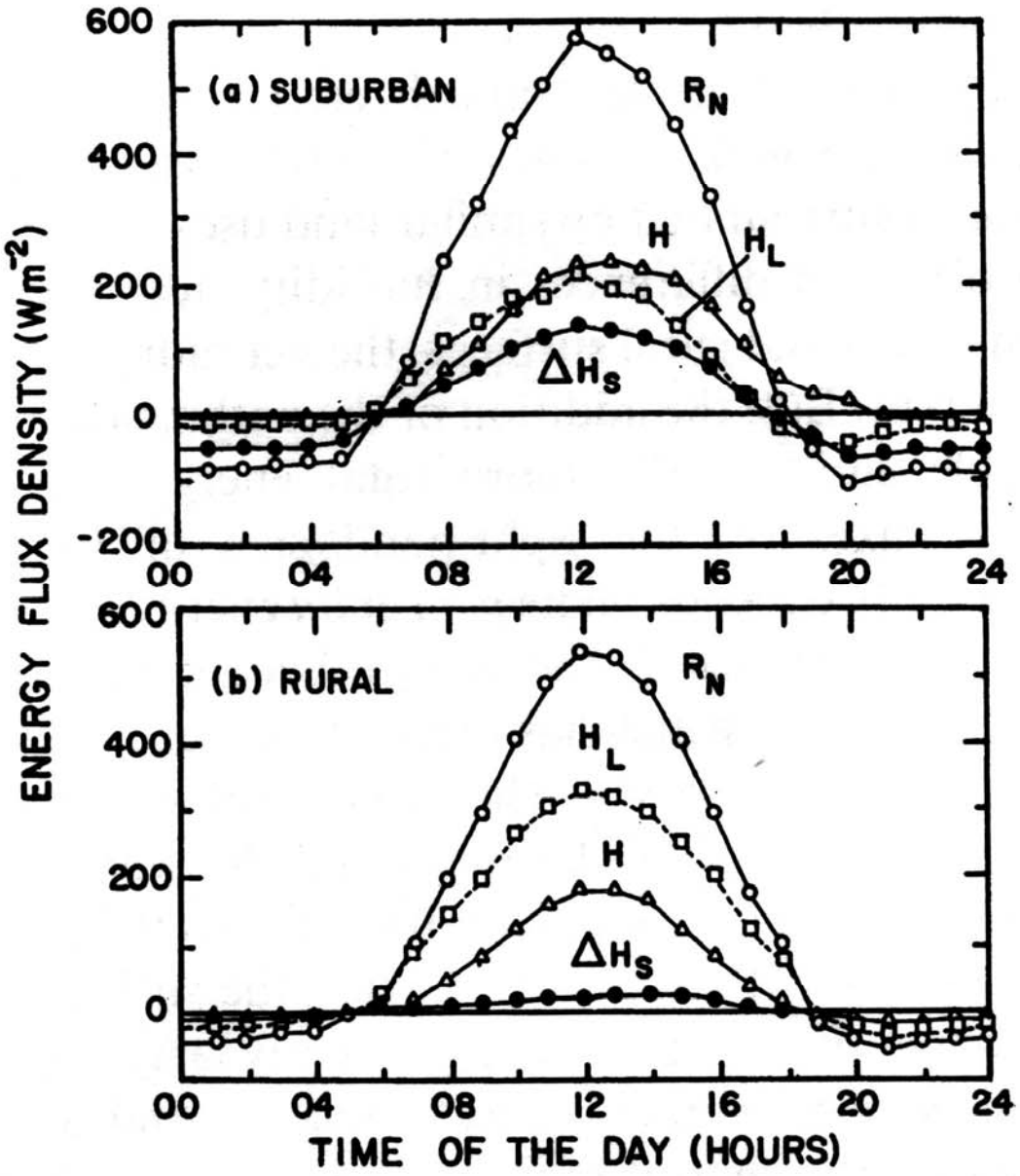

Figure 2.6 Monthly-averaged energy budgets at suburban and rural sites in Greater Vancouver, Canada, during summer. [From Oke (1987).]

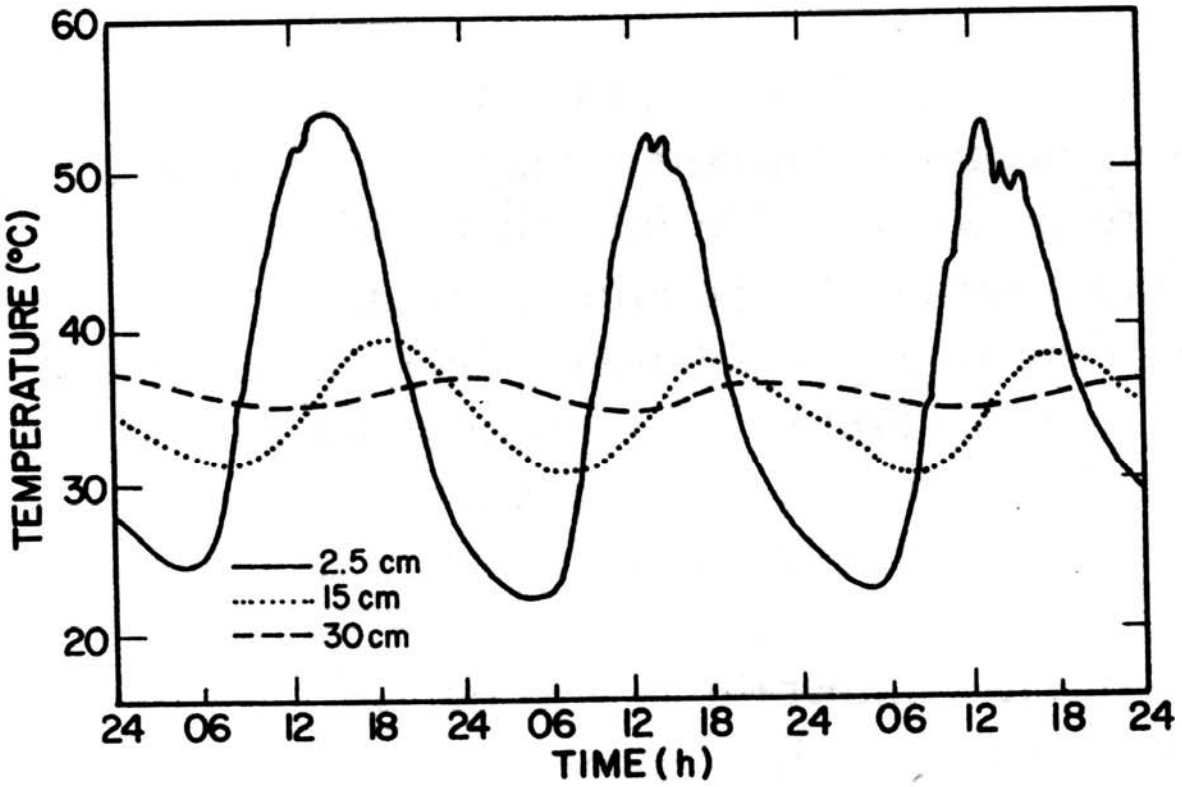

Figure 4.1 Observed diurnal course of subsurface soil temperatures at various depths in a sandy loam soil with bare surface. [From Deacon (1969); after West (1952).]

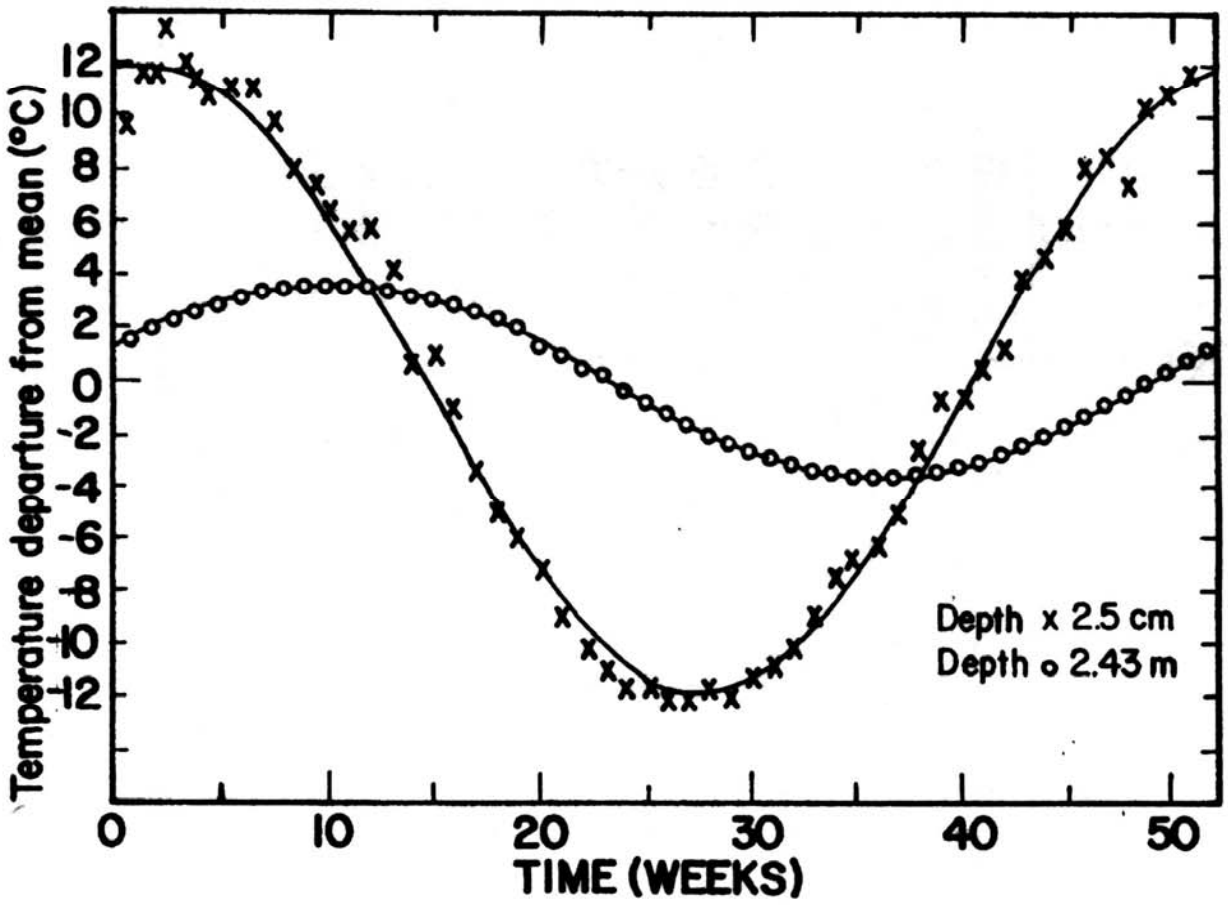

Figure 4.2 Annual temperature waves in the weekly averaged subsurface soil temperatures at two depths in a sandy loam soil. Fitted solid curves are sine waves. [From Deacon (1969); after West (1952).]

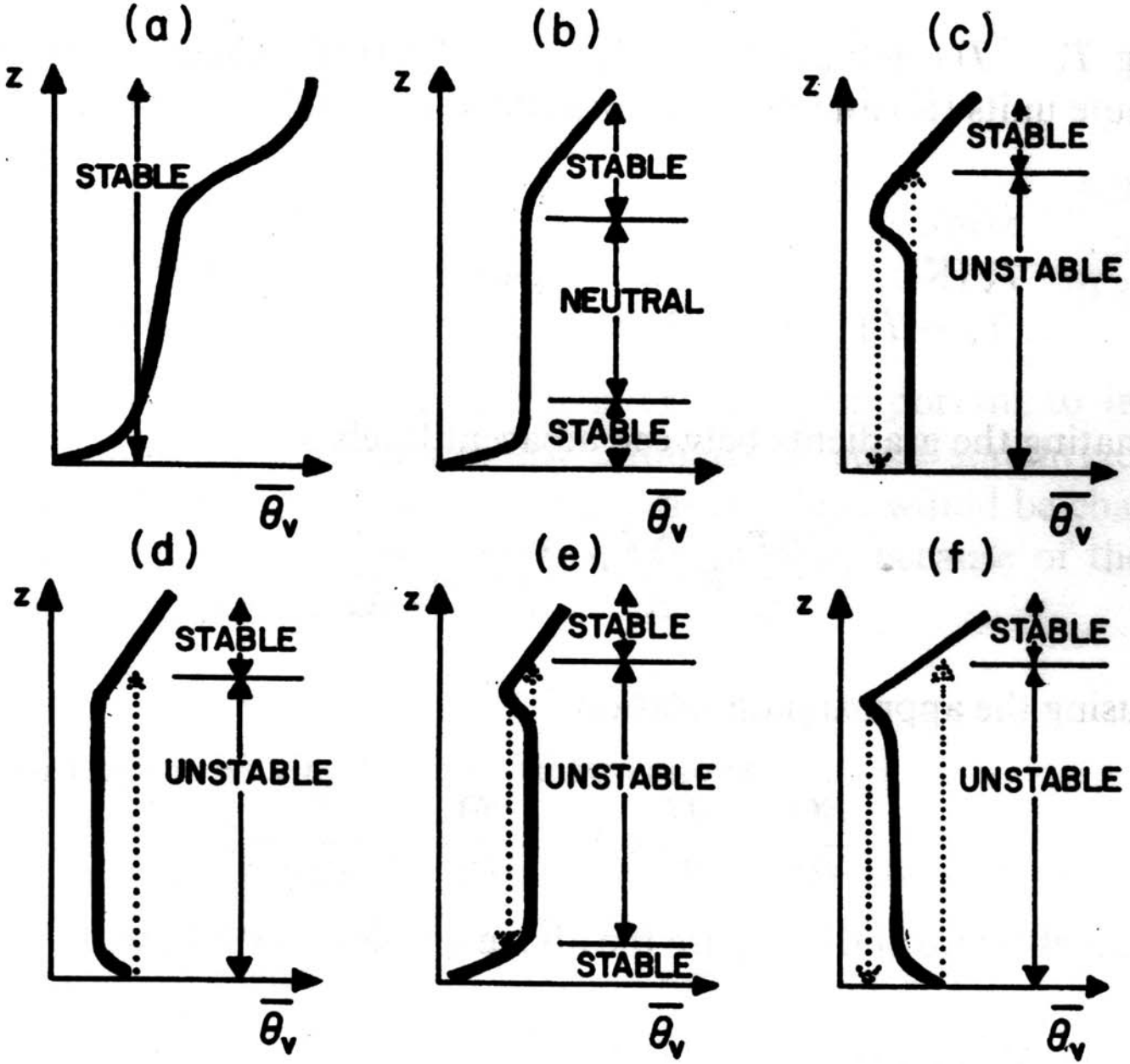

Figure 5.2 Nonlocal stability characterization for the various hypothetical virtual potential temperature profiles. [After Stull (1988).]

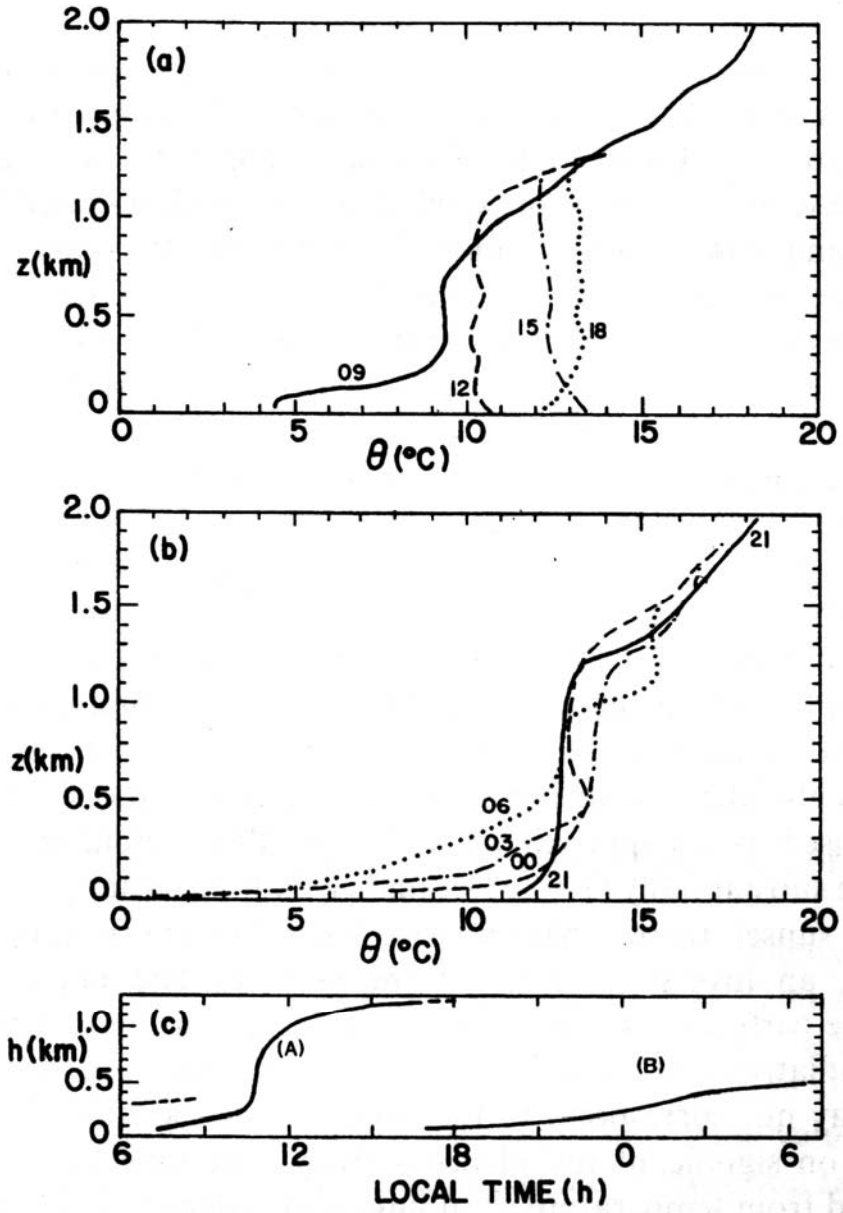

Figure 5.3 Diurnal variations of potential temperature profiles and inversion heights during (a) day 33 and (b) days 33–34 of the Wangara Experiment. (c) Curve A, inversion base height in the daytime CBL. Curve B, surface inversion height in the nighttime SBL. [After Deardorff (1978).]

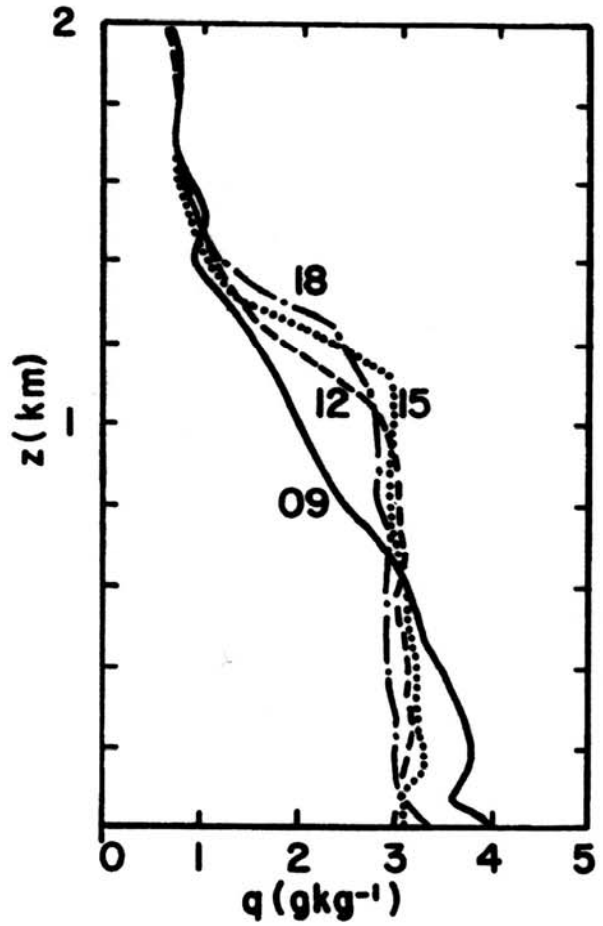

Figure 5.4 Diurnal variation of specific humidity profiles during day 33 of the Wangara Experiment. [From Andre *et al.* (1978).]

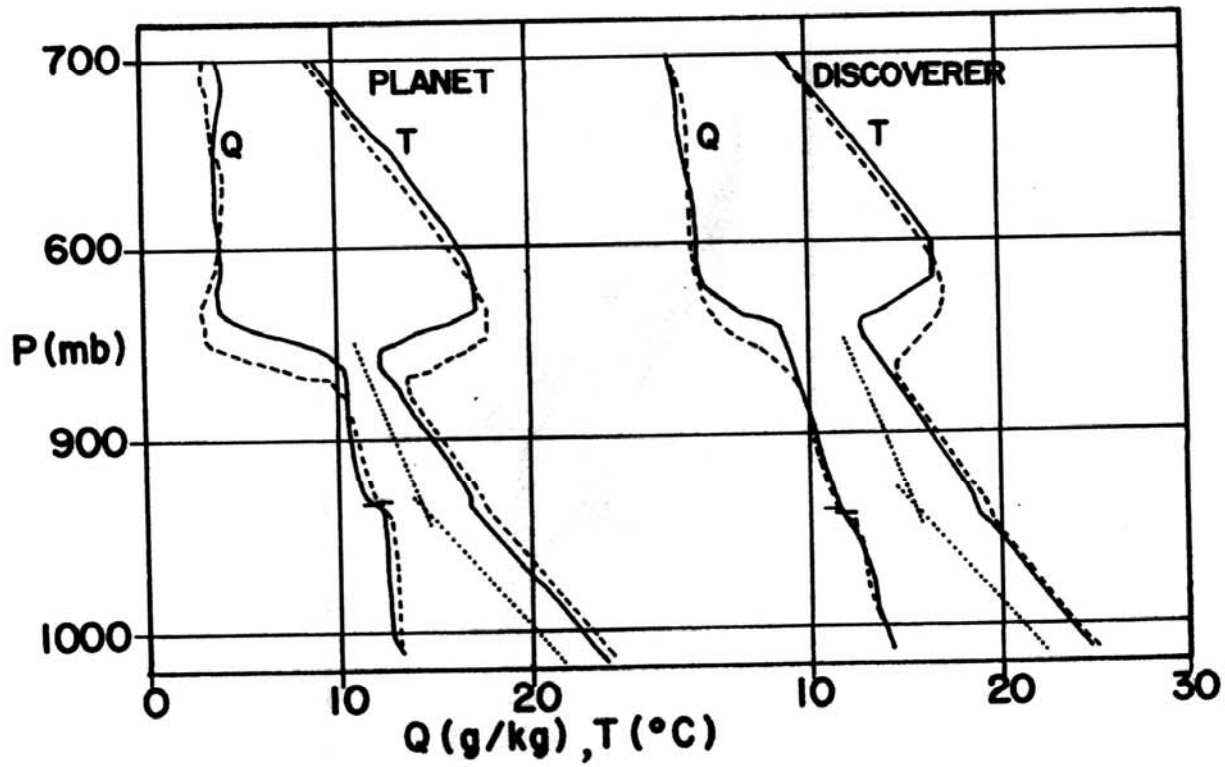

Figure 5.5 Observed mean vertical profiles of temperature and specific humidity at two research vessels during ATEX. First ('undisturbed') period: solid lines; second ('disturbed') period: dashed lines. The dotted lines indicate the dry adiabatic and saturated adiabatic lapse rates. [After Augstein *et al.* Copyright © (1974) by D. Reidel Publishing Company. Reprinted by permission.]

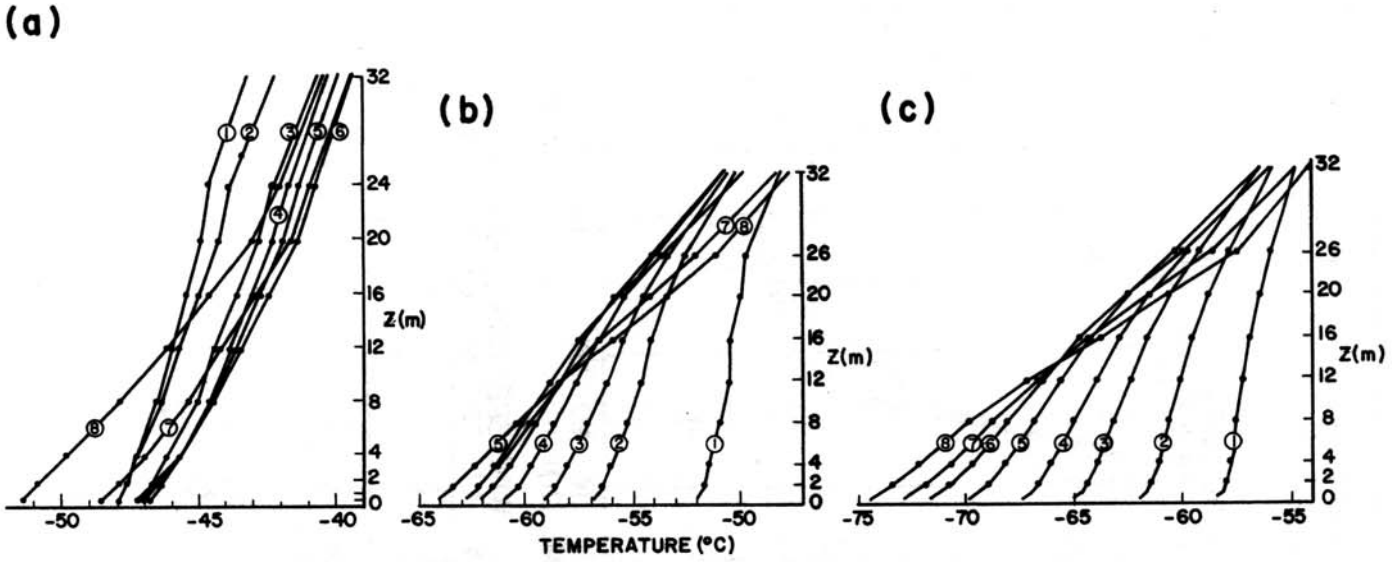

Figure 5.6 Observed mean temperature profiles in the surface inversion layer at Plateau Station, Antarctica, for three different periods grouped under different stability classes. (a) Sunlight periods, 1967; (b) transitional periods, 1967; (c) dark season, 1967. [After Lettau *et al.* (1977).]

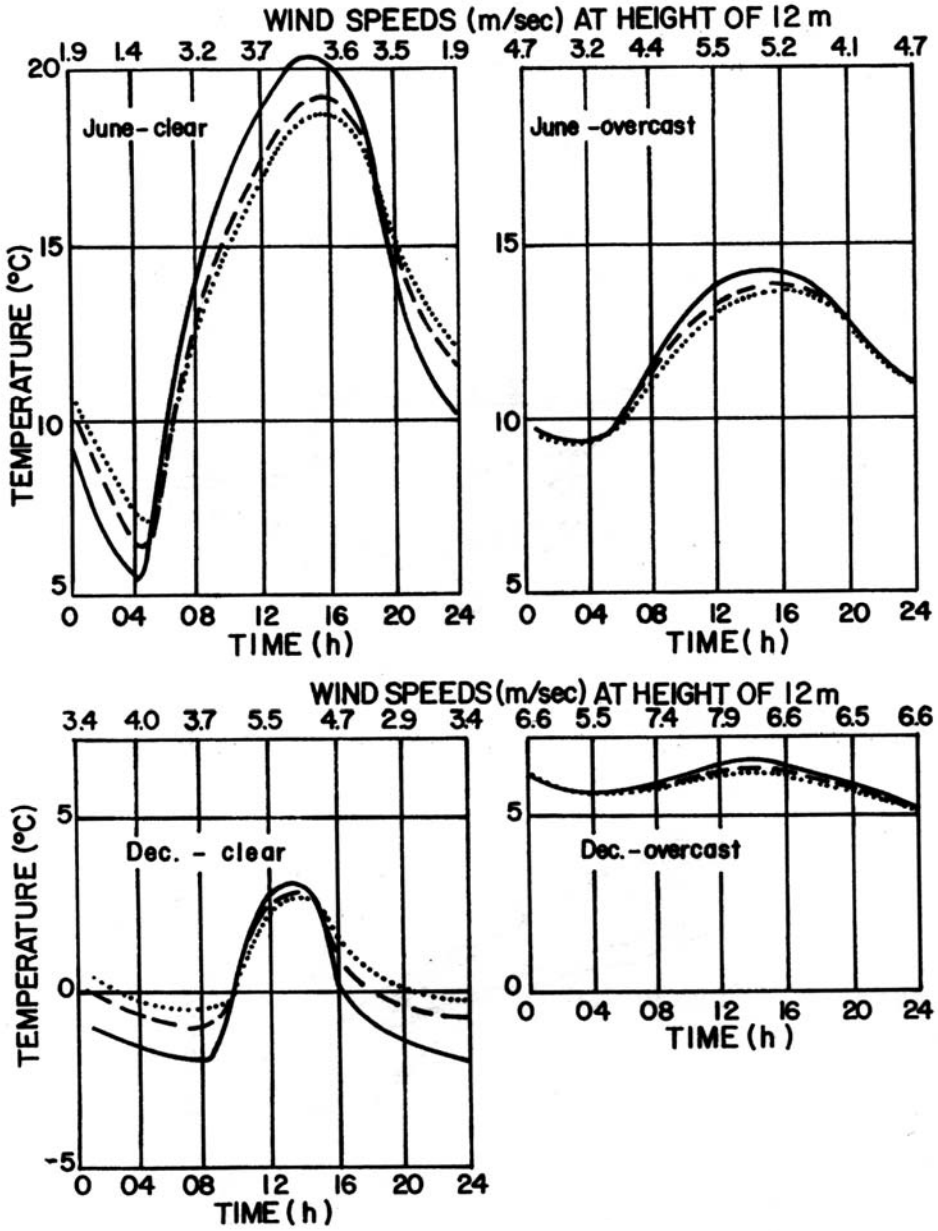

Figure 5.7 Diurnal variation of air temperature at three heights (solid lines: 1.2 m; dashed lines: 7 m; dotted lines: 17 m) over downland in Southern England for various combinations of clear and overcast days in June and December. Wind speeds at 12 m height are also indicated. [From Deacon (1969); after Johnson (1929).]

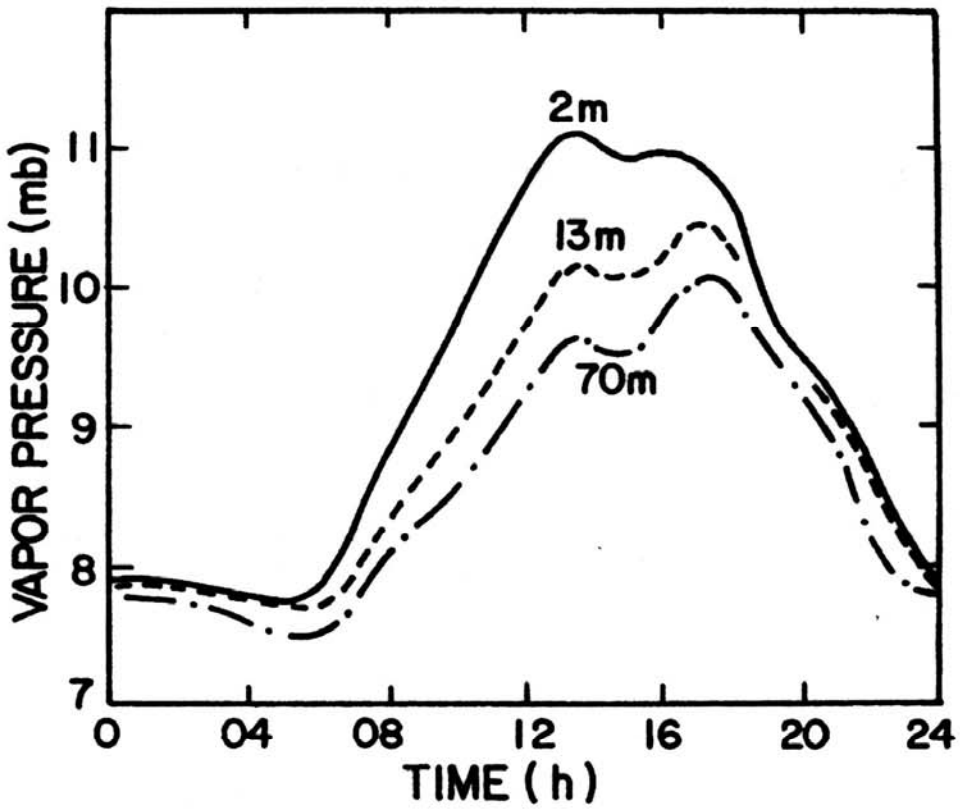

Figure 5.8 Diurnal variation of water vapor pressure at three heights at Quickborn, Germany, on clear May days. [From Deacon (1969).]

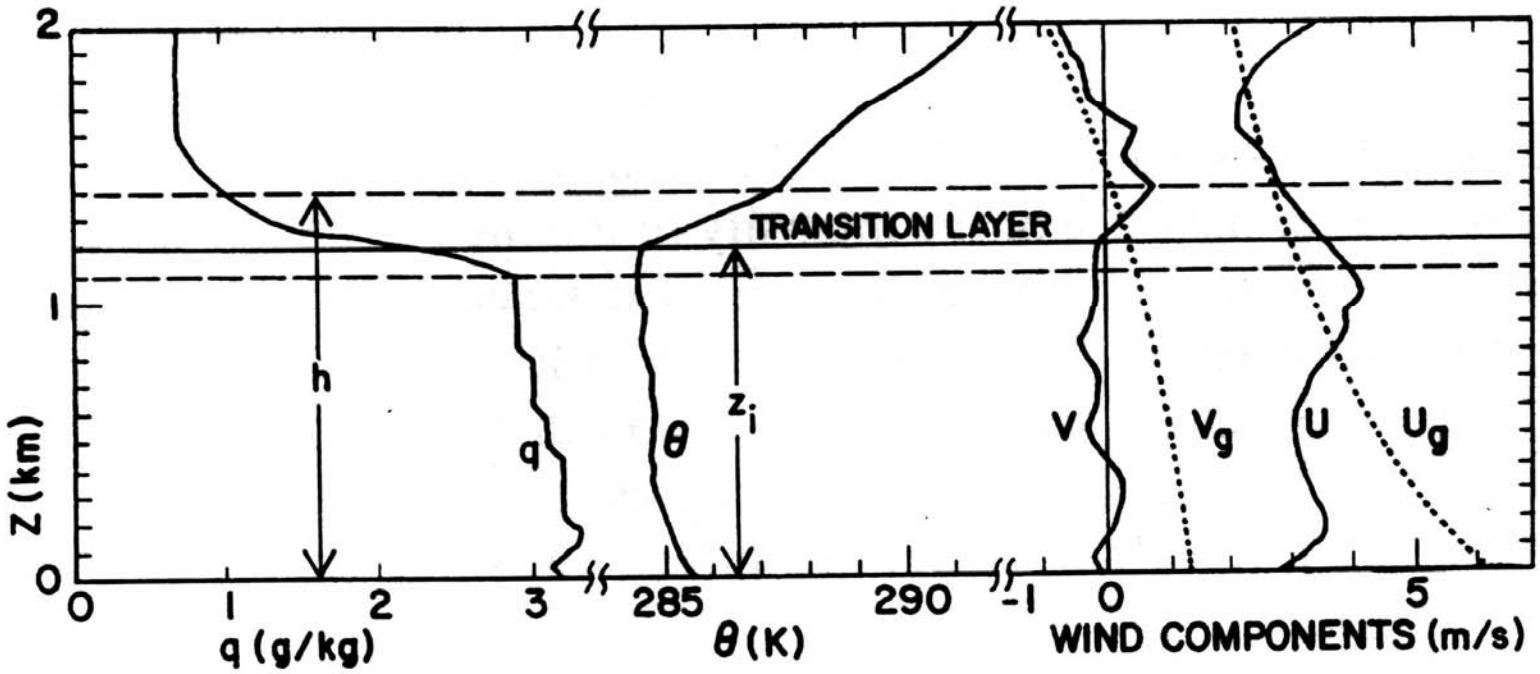

Figure 6.5 Measured wind, potential temperature and specific humidity profiles in the PBL under convective conditions on day 33 of the Wangara Experiment. [From Deardorff (1978).]

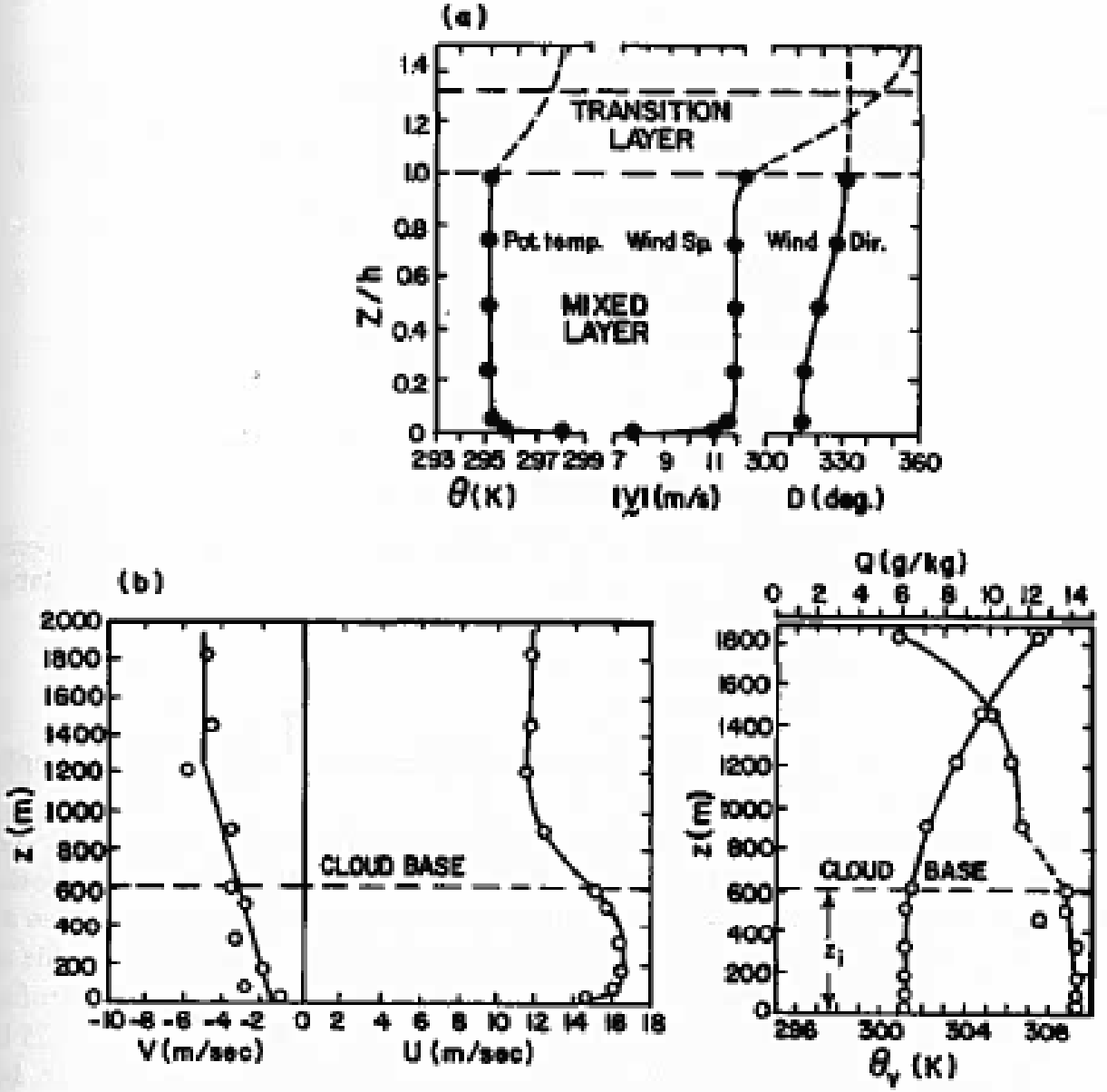

Figure 6.6 Observed vertical profiles of mean wind components, or wind speed and direction, potential temperature and specific humidity in the PBL. (a) Convective conditions overland. [After Kaimal *et al.* (1976).] (b) Unstable conditions over the ocean. [After Pennell and LeMone (1974).]

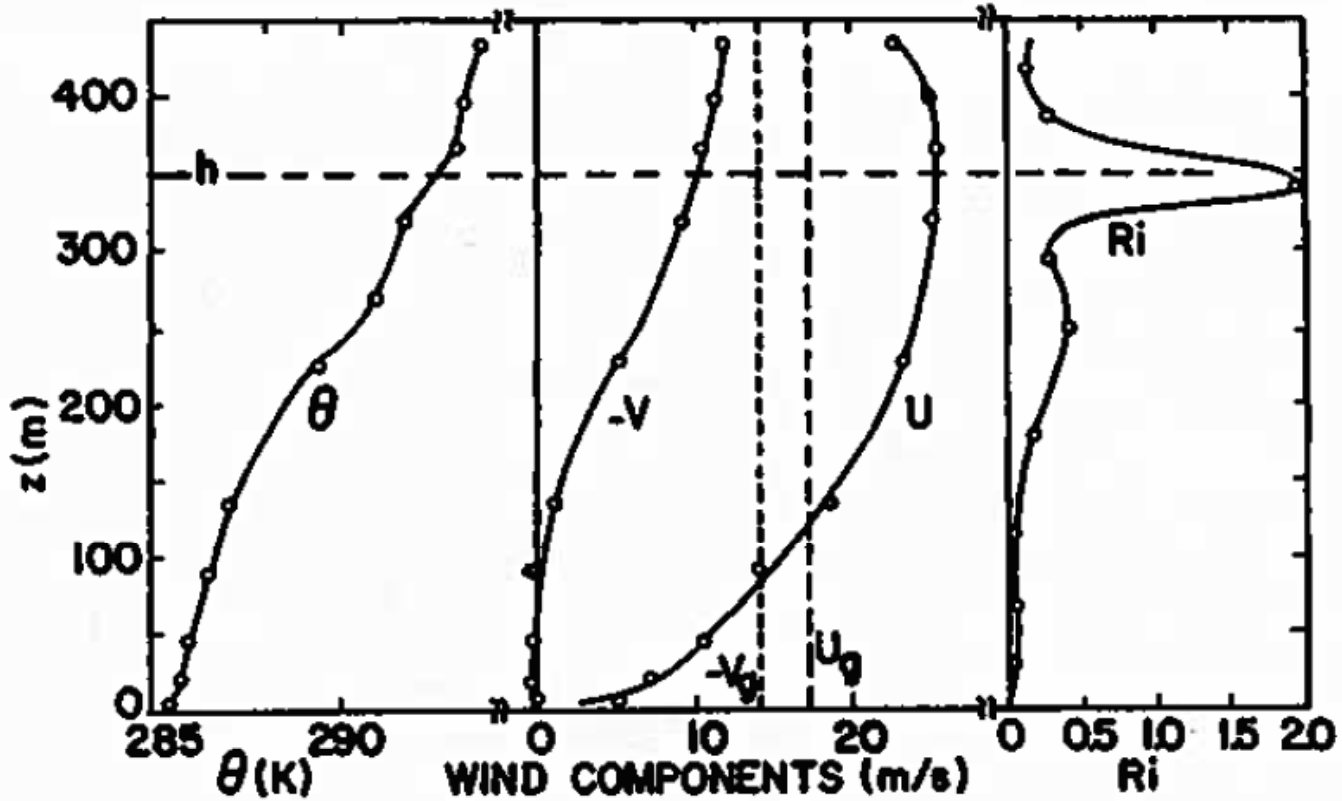

Figure 6.7 Observed vertical profiles of mean wind components and potential temperature and the calculated Ri profile in the nocturnal PBL under moderately stable conditions. [From Deardorff (1978); after Izumi and Barad (1963).]

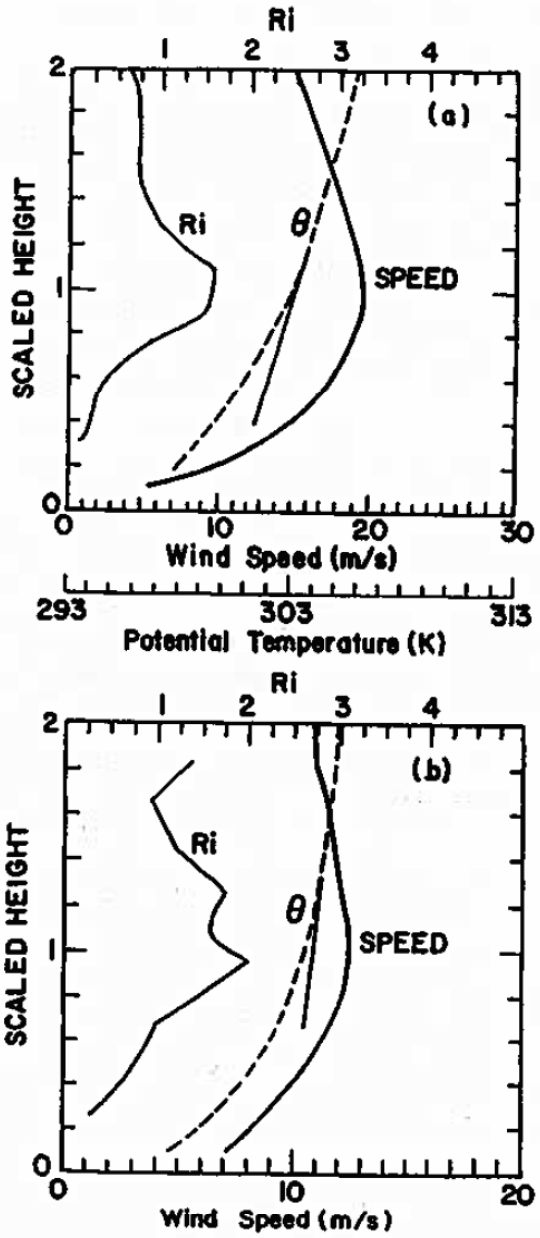

Figure 6.9 Composite profiles of wind speed, potential temperature and Richardson number scaled with respect to the low-level jet height at (a) O'Neill, Nebraska, during the Great Plains Experiment and (b) Hay, Australia, during the Wangara Experiment. [After Mahrt *et al.*

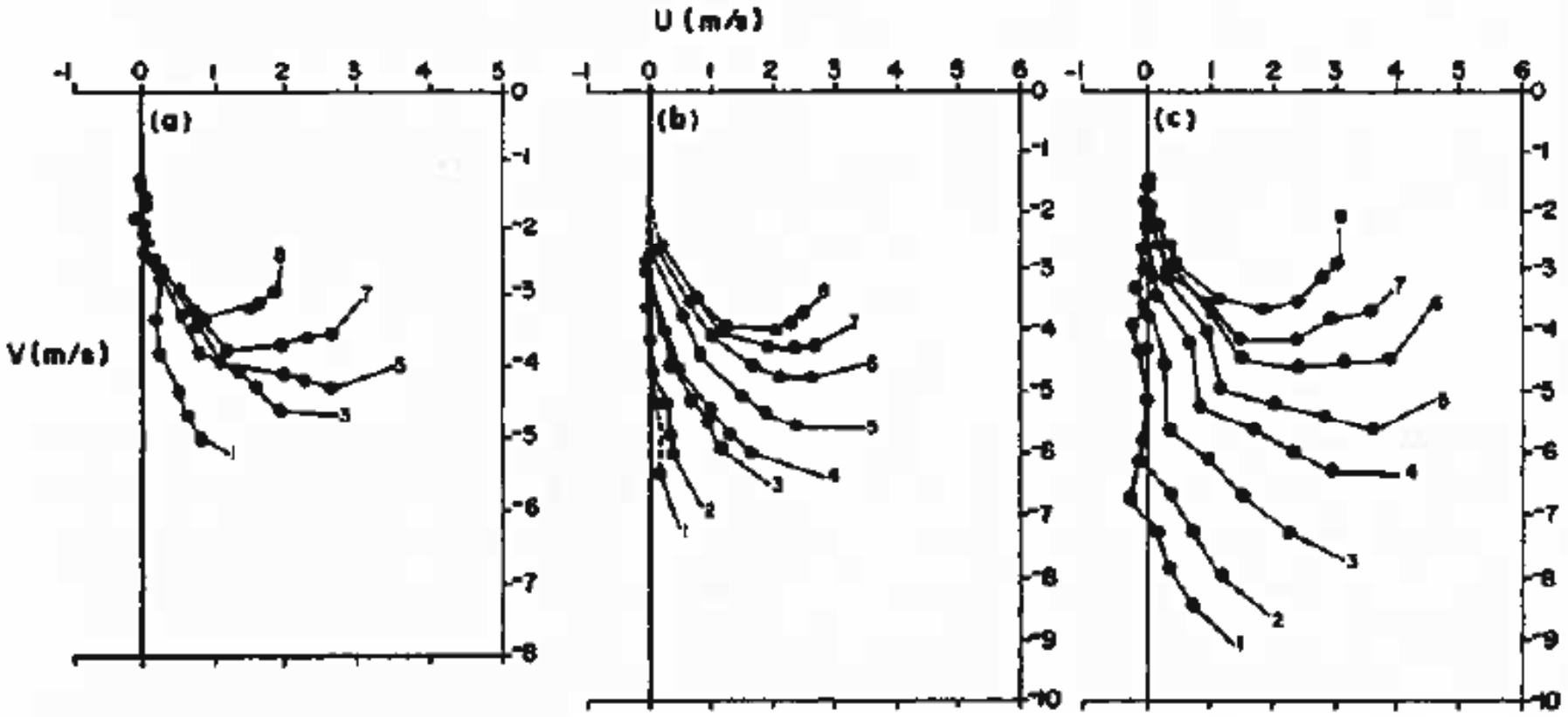

Figure 6.10 Averaged observed wind hodographs at Plateau Station, Antarctica, for (a) sunlight, (b) transitional, and (c) dark periods, grouped under different stability classes 1–8. Dots indicate ends of wind vectors at heights of 0.5, 1, 2, 4, 8, 12, 16, 20, 24, and 32 m. The components shown are in the so-called geotriptic coordinate system. [After Lettau *et al.* (1977).]

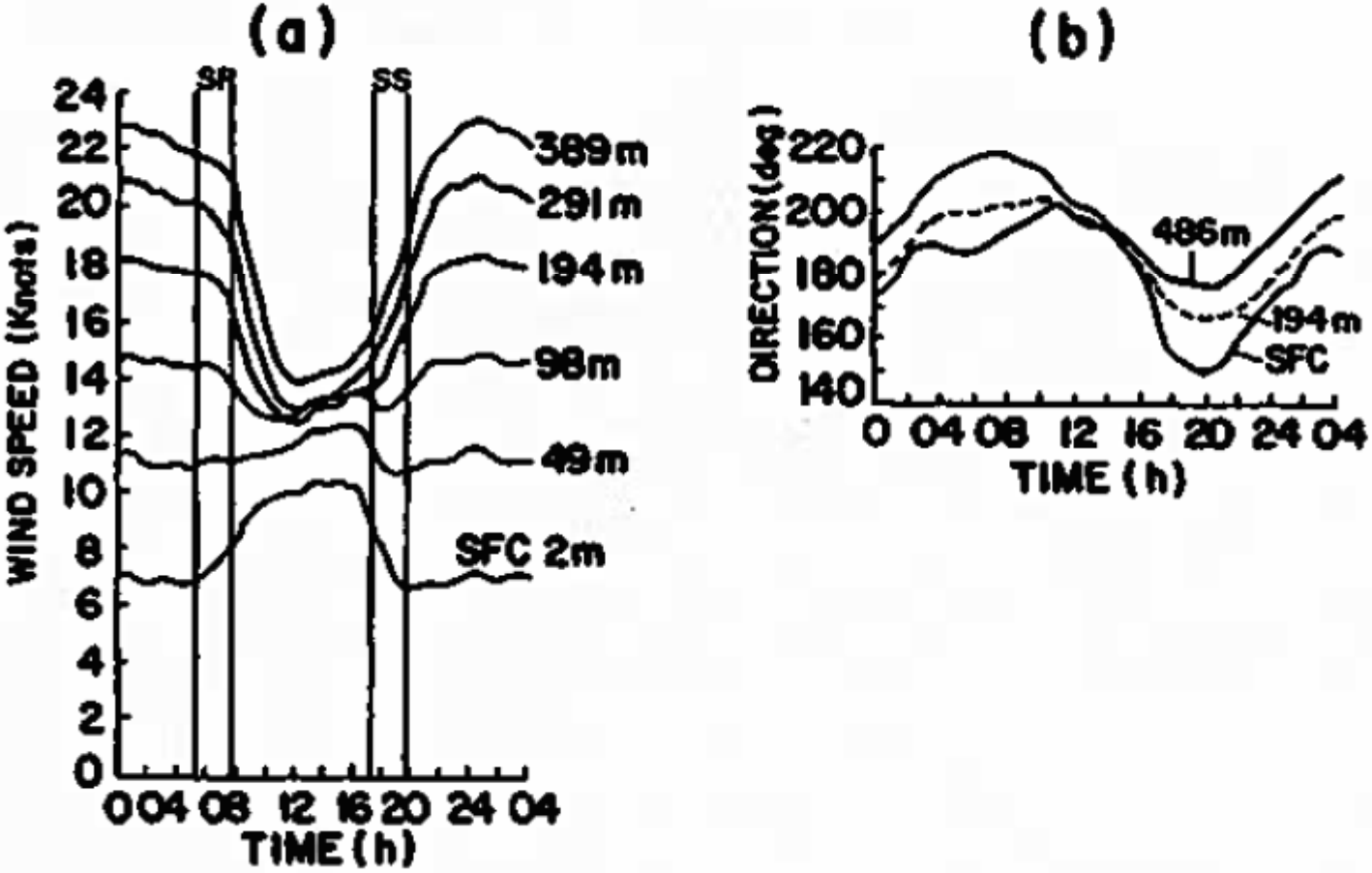

5.12 Diurnal variations of (a) mean wind speed and (b) mean wind direction, on ıal basis, for various height levels in the PBL near Oklahoma City, Oklahoma. Crawford and Hudson (1973).]

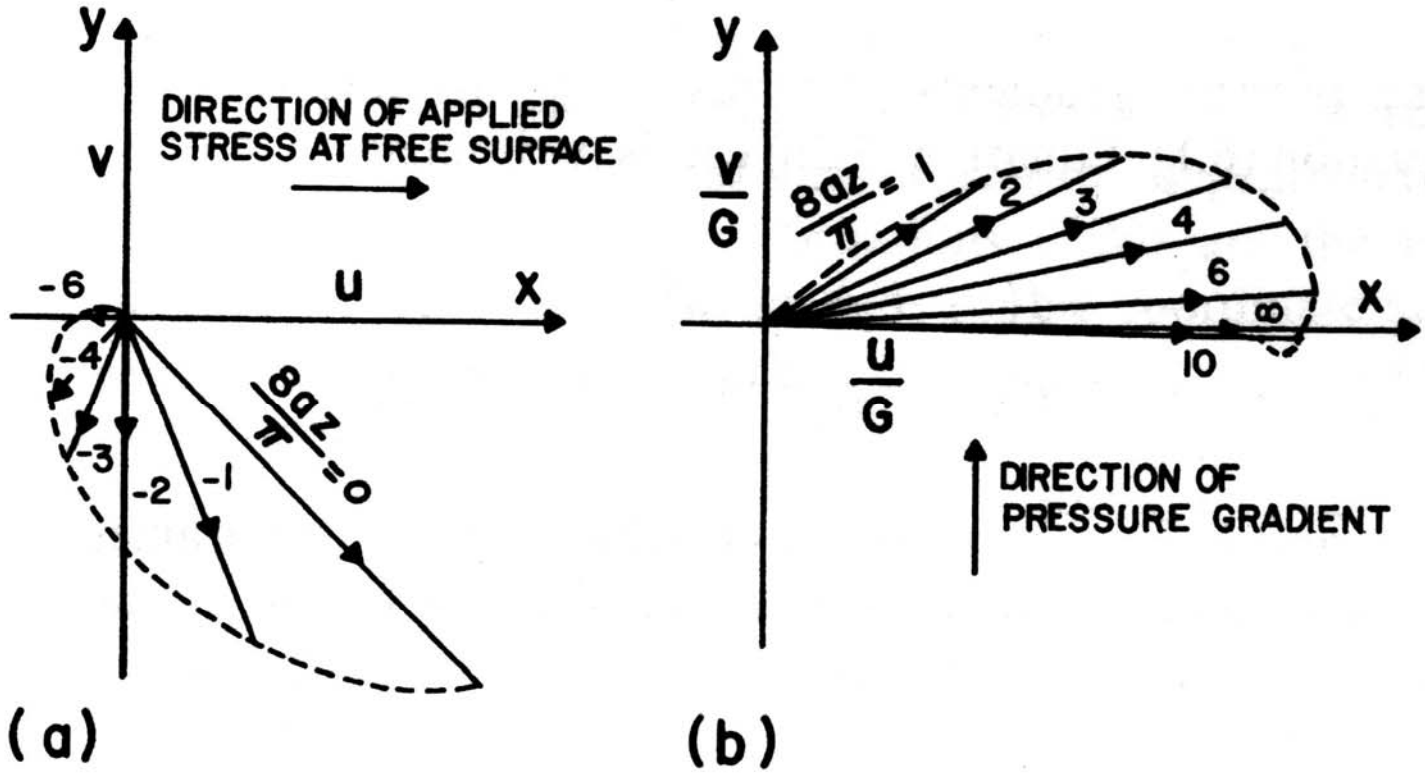

Figure 7.2 Velocity hodographs in laminar Ekman layers: (a) below free surface where tangential stress is applied; (b) above a rigid surface where a constant pressure gradient is applied. [From Batchelor (1970).]

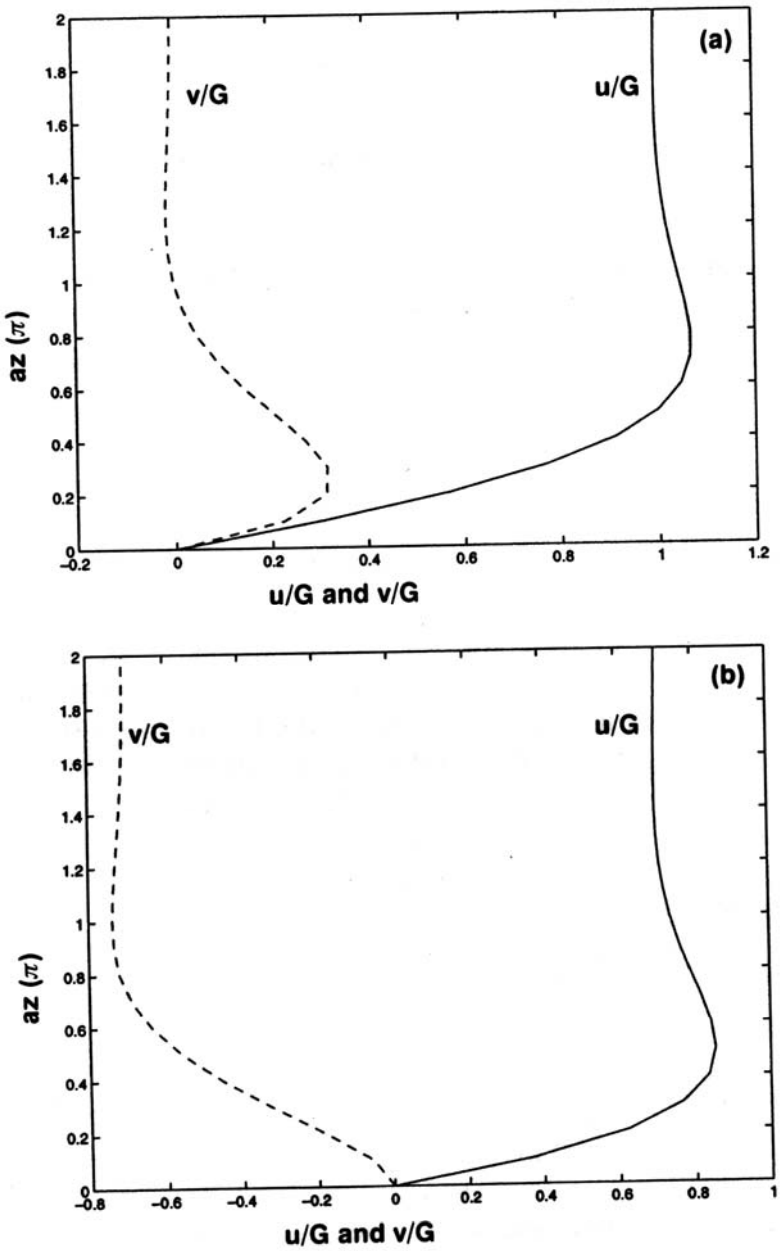

Figure 7.3 Horizontal velocity component profiles in the laminar Ekman layer in (a) the geostrophic coordinate system, and (b) the surface-layer coordinate system. Velocity components are normalized by geostrophic wind speed G, while az is the normalized height.

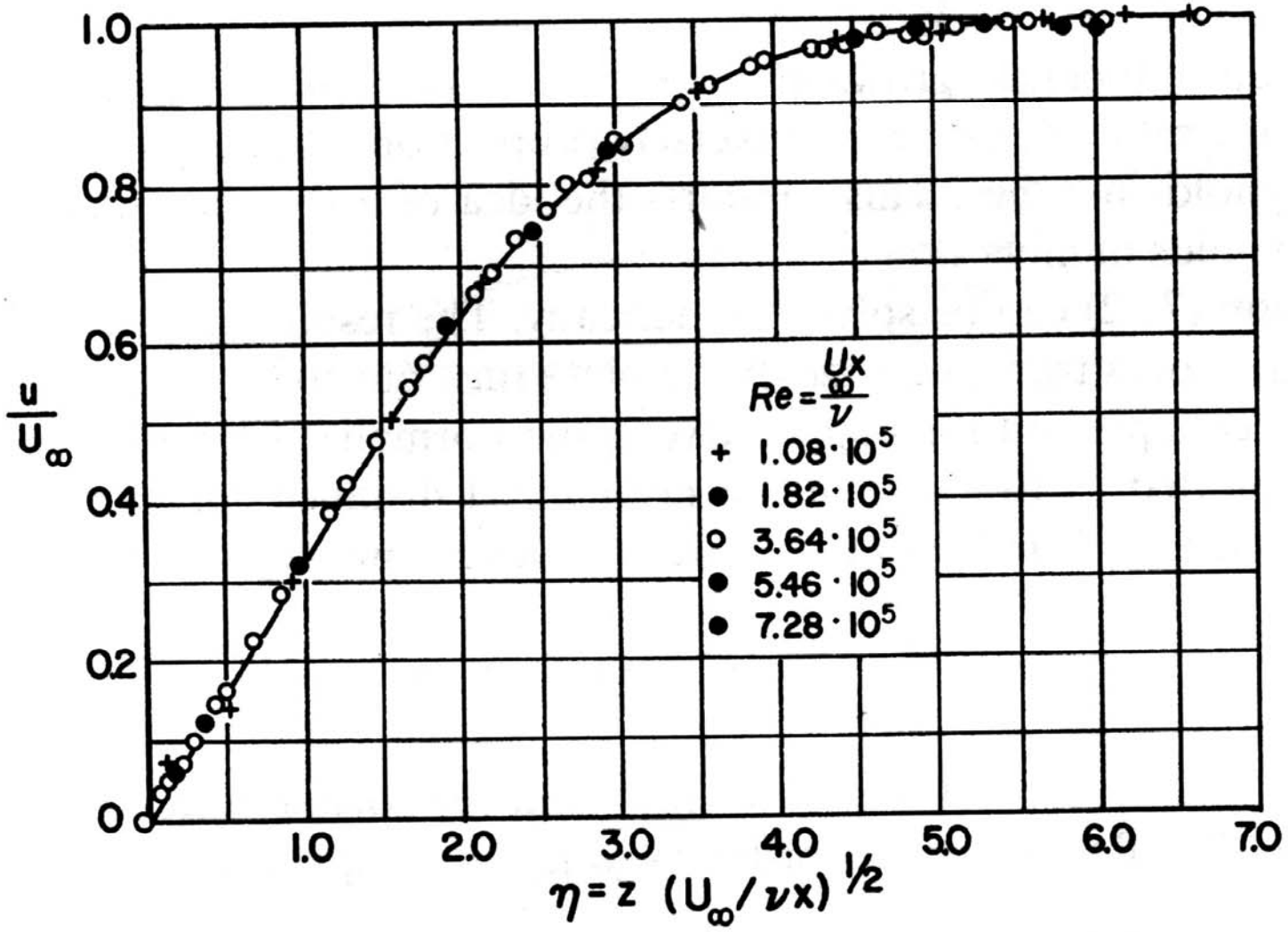

Figure 7.5 Comparison of theoretical and observed velocity profiles in the laminar flat-plate boundary layer. [From Schlichting (1960).]

Equations of motion

$$\frac{Du}{Dt} - fv = -\frac{1}{\rho}\frac{\partial p}{\partial x} + \nu\nabla^2 u$$

$$\frac{Dv}{Dt} + fu = -\frac{1}{\rho}\frac{\partial p}{\partial y} + \nu\nabla^2 v$$

$$\frac{Dw}{Dt} + g = -\frac{1}{\rho}\frac{\partial p}{\partial z} + \nu\nabla^2 w$$

$$\frac{\partial U}{\partial x}+\frac{\partial V}{\partial y}+\frac{\partial W}{\partial z}=0$$

$$\frac{\partial U}{\partial t}+U\frac{\partial U}{\partial x}+V\frac{\partial U}{\partial y}+W\frac{\partial U}{\partial z}=fV-\frac{1}{\rho_0}\frac{\partial P_1}{\partial x}+\nu\nabla^2 U - \left(\frac{\partial \overline{u^2}}{\partial x}+\frac{\partial \overline{uv}}{\partial y}+\frac{\partial \overline{uw}}{\partial z}\right)$$

$$\frac{\partial V}{\partial t}+U\frac{\partial V}{\partial x}+V\frac{\partial V}{\partial y}+W\frac{\partial V}{\partial z}=-fU-\frac{1}{\rho_0}\frac{\partial P_1}{\partial y}+\nu\nabla^2 V - \left(\frac{\partial \overline{uv}}{\partial x}+\frac{\partial \overline{v^2}}{\partial y}+\frac{\partial \overline{vw}}{\partial z}\right) \tag{9.8}$$

$$\frac{\partial W}{\partial t}+U\frac{\partial W}{\partial x}+V\frac{\partial W}{\partial y}+W\frac{\partial W}{\partial z}=\frac{g}{T_0}T_1-\frac{1}{\rho_0}\frac{\partial P_1}{\partial z}+\nu\nabla^2 W - \left(\frac{\partial \overline{wu}}{\partial x}+\frac{\partial \overline{wv}}{\partial y}+\frac{\partial \overline{w^2}}{\partial z}\right)$$

$$\frac{\partial \Theta}{\partial t}+U\frac{\partial \Theta}{\partial x}+V\frac{\partial \Theta}{\partial y}+W\frac{\partial \Theta}{\partial z}=\alpha_h\nabla^2\Theta-\left(\frac{\partial \overline{u\theta}}{\partial x}+\frac{\partial \overline{v\theta}}{\partial y}+\frac{\partial \overline{w\theta}}{\partial z}\right)$$

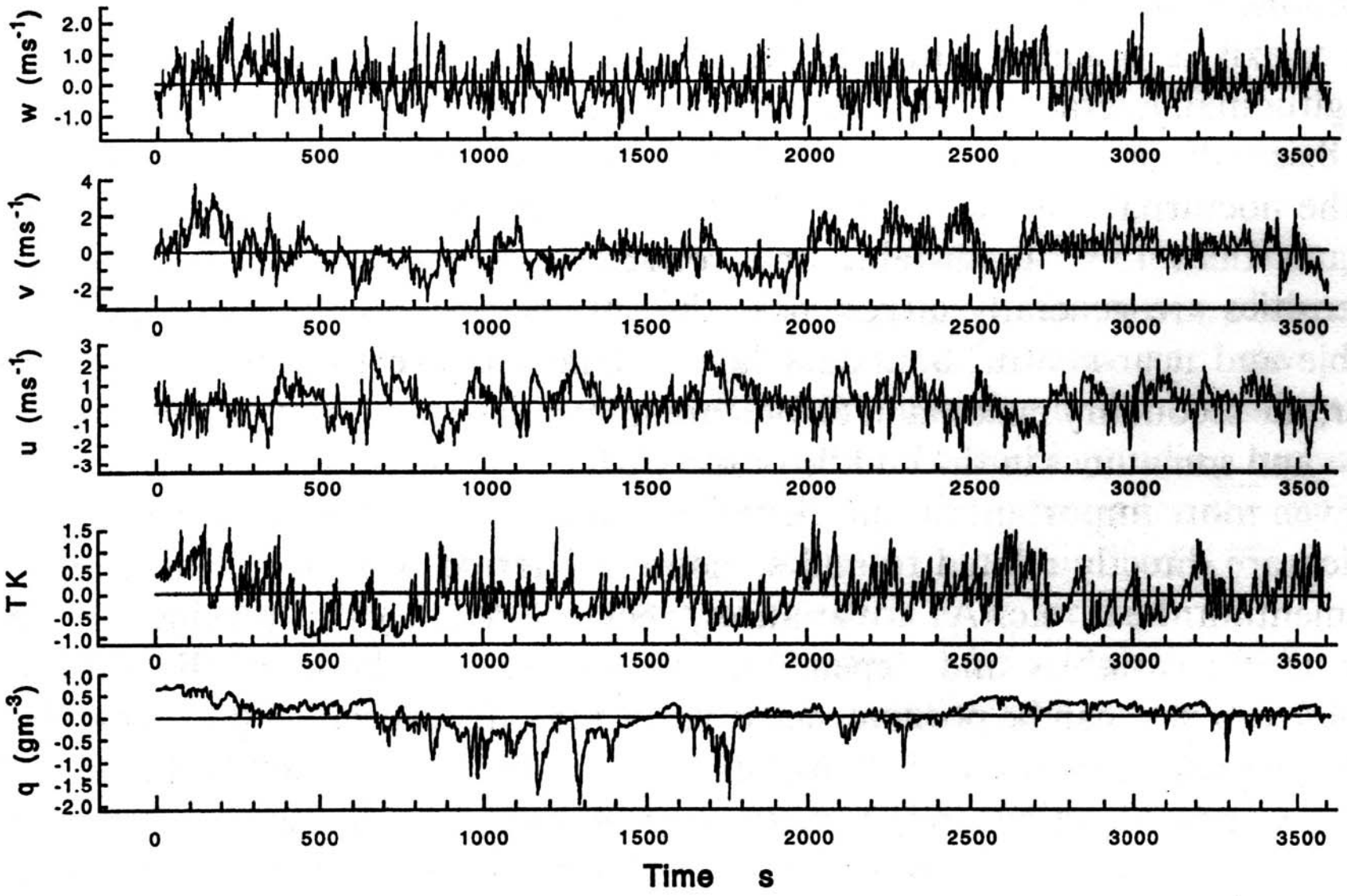

Figure 8.1 Observed time series of velocity, temperature, and absolute humidity fluctuations in the atmospheric surface layer at a suburban site in Vancouver, Canada, during moderately unstable conditions. [From Roth (1991).]